IMPLEMENTATION OF AERO-ELASTIC CAPABILITIES IN A LBM FLOW SOLVER: APPLICATION TO A LOW-REYNOLDS ROTOR FOR MICRO-AIR VEHICLES

Antonio ALGUACIL , Antonio.ALGUACIL-CABRERIZO@student.isae-supaero.fr, ISAE-Supaero (France)
Thierry JARDIN , thierry.jardin@isae-supaero.fr, ISAE-Supaero (France)
Nicolas GOURDAIN , nicolas.gourdain@isae-supaero.fr, ISAE-Supaero (France)

Abstract
Micro air vehicles (MAVs) are used both for civil (rescue missions) and military (surveillance, recognition) applications. However the aerodynamic performance of the propeller is known to be lower than for classical large rotors, due to leading edge vortex occurring at low Reynolds number flows. Such rotors can also exhibits a flexible behaviour due to the material used to build the blades, making the prediction of aerodynamic performance challenging for numerical flow solvers. A potential way to improve the rotor performance is also to take advantage of the flow unsteadiness, by imposing an unsteady forced motion, like a periodic variation of the rotor pitch. There is thus a need to develop aero-elastic capabilities in numerical flow solvers, which is the main objective of this paper. The method relies on the implementation of Fluid-Structure Interaction (FSI) capabilities in a Lattice-Boltzmann flow solver, in order to take advantage of the flexibility allowed by the immersed boundary approach. FSI capabilities are implemented in a monolithic fashion, using generalised coordinates to represent the blade as a flexible beam. Two sets of simulations are performed: a) with a forced motion and b) by coupling the flow with the equation of the dynamics. Results show that a forced motion has a good potential to increase the rotor thrust but significant improvements should yet to be done to reduce the over-power consumed by the forced motion. While dynamic flapping has a negligible influence on the flow, dynamic pitching has the potential to moderately modify the pressure distribution at the trailing edge. However its impact on the rotor performance is weak (less than 0.5% on the thrust).

SYMBOLS AND ABBREVIATION

C :	Blade chord	m
C_p :	Pressure coefficient	-
C_Q :	Torque coefficient	-
C_T :	Thrust coefficient	-
D :	Rotor diameter	-
R :	Radius at the rotor tip	m
V_i :	Induced velocity	$m.s^{-1}$
r :	spanwise coordinate	m
α :	pitching angle	rad
β :	flapping angle	rad
ω :	surging angle	rad
$\dot{\omega}$:	Secondary rotation velocity	$rad.s^{-1}$
Ω :	Main rotation velocity	$rad.s^{-1}$

1. INTRODUCTION

The thrust and torque are parameters of paramount importance when designing a propeller, both for payload and efficiency. Usually, the thrust and torque coefficients are estimated for a propeller as a function of the incidence angle α and the rotation speed Ω, such that $C_T = k.f(\alpha, \Omega)$

with k a coefficient that depends on the considered geometry (for example $k = 2\pi$ in the case of a thin 2D airfoil). Major efforts have been done recently to improve the performance of rotor by optimizing the design of blades under steady flow conditions. However, the possibility to increase the rotor performance by taking advantage of unsteady flow effects has received less attention. Typically, the thrust and torque coefficients could be written in a more general manner, as $C_T = k.f(\alpha, \beta, \omega, \dot{\alpha}, \dot{\beta}, \dot{\omega})$, with α, β, ω, the three possible solid rotation angles and $\dot{\alpha}$, $\dot{\beta}$, $\dot{\omega}$, their corresponding angular velocities.

A rotor blade can experience different type of oscillating motions as a response to unsteady aerodynamic forces and fluid-structure interactions. As a first approach, these motions can be described as three solid rotations about axis oriented radially, azimuthally and perpendicularly to the mean blade path, referred to as pitching, flapping and surging motions. For low amplitude oscillations, in the linear, attached flow regime, the resulting unsteady aerodynamic forces and blade motion can be predicted using conventional, potential flow theory[1,2]. However, when the effective angle of attack of the blade exceeds the static stall angle of the airfoil blade section, and leading edge flow separation occurs, inducing highly non-linear phenomena, then high-fidelity numerical simulations or measurements are required to predict the complex physics that lead to drastic changes in aerodynamic performance of the blade. In these specific cases, the blade motion is highly correlated with the time scale of large scale coherent vortices being formed at the leading edge of the blade.

While an uncontrolled blade motion most presumably results in a decrease in aerodynamic performance, a controlled (forced) motion could potentially have a beneficial impact. This was first suggested by Holten[3] who introduced the concept of flapping rotor on a medium scale rotorcraft model: the flapping motion was powered while the rotating motion was induced by the flapping motion. Such a mechanism has the potential to annihilate the rotating reaction torque, eliminating the need for a tail rotor. This concept was further investigated on a micro-scale rotor[4,5], sometimes with the ability to couple both flapping and (active or passive) pitching motions, and with powered or induced rotation. It recently gained considerable interest with a significant amount of work[6,7,8,9,10,11,12]. Overall, these studies suggest that thrust could significantly be enhanced with respect to conventional rotors, yet with lower efficiency. Similar conclusions were raised for a pitching rotor[13], where the rotating blade undergoes a pitching motion about a spanwise axis (without flapping motion).

The objective of the present work is thus to study the influence of unsteady flow effects on the global performance of a propeller, adapted to the propulsion of micro-air vehicles (MAV). Several challenges are associated to this objective: the numerical prediction of such unsteady flows (leading edge vortex, massive separation, turbulence) remains difficult and the unsteady displacement of the blade (due to forced motion or dynamic response to unsteady aerodynamic forces) require adapted numerical methods. To address these difficulties, the present work relies on the development of Fluid-Structure Interactions (FSI) capabilities in a Lattice-Boltzmann Method, to take advantage of the immersed boundary approach. The first part of this paper present the implementation of such FSI, by coupling the equation of the dynamics with the aerodynamic flow solver. Then, these methods are used to study the influence of forced motions, as flapping, pitching and surging, on the rotor performance. Finally, the analysis is extended to cases where blade oscillating motions are induced by fluid-structure interactions.

2. TEST CASE AND NUMERICAL METHODS

2.1. Geometry and operating conditions

The test case is a 2-bladed rotor of diameter D=0.250m, operating in hover and designed to be representative of a typical MAV propeller. The main characteristics of the rotor are reported in Table 1. The rotor is composed of two untwisted flat plates. The span R, chord C and thickness h of the blade are 0.100m, 0.025m and 0.001m, respectively. The distance between the hinge of the two blades is set to two chords. The angle of attack of the profiles is initially set to $\alpha_0 = 15°$, as shown in Fig. 1. The rotation speed Ω of the rotor is set to 3,960 RPM, corresponding to a Mach number at tip of 0.151. The data presented in this paper are normalized using a standard atmosphere, with temperature T_0=293 K and static pressure p_0=101,325 Pa.

Table 1: Characteristics of the rotor test case.

Number of blades	2
Rotation rate Ω	414.69 rad.s^{-1}
Rotor diameter, D	0.250 m
Blade chord, C	0.025 m
Blade span, R	0.100 m
Blade thickness, h	0.001 m
Reynolds number, Re	0.86×10^5

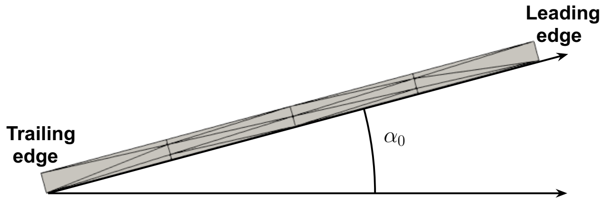

Figure 1: Lateral view from the hub of the blade.

2.2. Structural properties of the blade

Regarding the dynamic response of the blade to aerodynamic forces, the main rotations of interest are pitch (α) and flap (β). As a first approximation, the blade is considered as a flexible 1D beam. To predict the dynamic behaviour of the blade, it is thus necessary to estimate the values of rotational stiffness and moment of inertia related to the blade. The dimensions of the blade are R, C and h, as reported in Table 1. The blade is made of epoxy ($\rho_S = 1.5 \times 10^3\ kg.m^{-3}$) and is assumed to be homogeneous. Using solid cuboid formulas and Steiner' s theorem[14] the moment of inertia for pitch and flap writes, respectively, as

$$I_{pitch} = I_\alpha = \frac{1}{12} m_S \left(C^2 + h^2\right) + m_S \left(\frac{C}{4}\right)^2 \tag{1}$$

$$I_{flap} = I_\beta \simeq \frac{1}{12} m_S R^2 + m_S \left(\frac{R}{2} + l_{off}\right)^2 \tag{2}$$

with $m_S = 3.8 \times 10^{-3} kg$ the mass of a blade and l_{off} the distance between the main rotation axis and the hinge. The calculation of the stiffness K relies on a beam approximation ($K = G.J/L$), with G the shear modulus and J the polar moment of area given by

$$J_{pitch} = J_\alpha = \frac{1}{12} hC \left(h^2 + C^2\right) + hC \left(\frac{C}{4}\right)^2 \tag{3}$$

and

$$J_{flap} = J_\beta = \frac{hR}{12} \left(h^2 + R^2\right) + hR \left(\frac{R}{2} + l_{off}\right)^2 . \tag{4}$$

The stiffnesses in pitching K_α and flapping K_β are then estimated considering the shear modulus of epoxy ($G_{epoxy} = 1.25$ GPa), as shown in Table 2.

Table 2: Structural properties of a blade.

	Pitch	Flap
Moment of inertia I, kg.m^2	$2.9\ 10^{-7}$	$2.8\ 10^{-5}$
Polar moment of area J, m^4	$2.3\ 10^{-9}$	$6.5\ 10^{-7}$
Stiffness K, N.m	30	8100

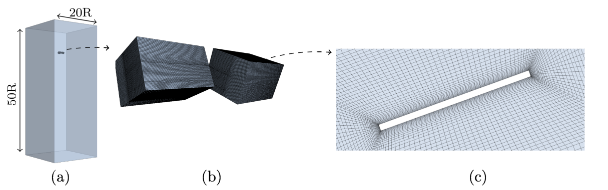

Figure 2: View URANS grid.

2.3. Unsteady RANS

The three-dimensional Unsteady Reynolds-Averaged Navier-Stokes equations (URANS) are solved under their incompressible form using StarCCM+ commercial code. An overset grid approach is used that allows each blade mesh to move following prescribed rotating and sinusoidal pitching motions within a stationnary background mesh. The structured mesh consists of 4.7 million hexahedral cells (0.9 million for each blade mesh and 2.9 millions for background mesh) enclosed within a box domain of width 20R and height 50R (see Fig. 2). The boundary conditions upstream and downstream of the rotor are implemented as pressure Dirichlet conditions while the periphery of the domain is defined using a slip-wall condition. The blades are modelled as non-slip surfaces. Blade mesh is moved with a time step that meets the Courant-Friedrichs-Lewy condition. Therefore, the time step is adjusted to pitching motion parameters with at least 720 time steps per rotating period. Both spatial and temporal discretizations are achieved using second-order schemes. Momentum and continuity equations are solved in an uncoupled manner using a predictor-corrector approach. Finally, the Spalart-Allmaras model is employed for turbulence closure with maximum y^+ values on the order of 6.

2.4. LES-LBM

The Large-Eddy Simulation (LES) is performed by means of a Lattice-Boltzmann Method (LBM), which already demonstrated its capability to solve flows for low-Reynolds number rotors[15]. Beyond its computational performance, the main advantage of

LBM is that the method is stable without artificial dissipation, which makes the method equivalent to solve the Navier-Stokes equations with a high-order numerical scheme. Its drawback is that it requires the use of Cartesian grids. To counter-balance this limitation, the walls are represented through an immersed boundary approach[16]. The main advantage of this method is that the position of the wall can be easily updated at each time step, which makes this technique well suited to unsteady blade motion. The LBM considers the discrete Boltzmann equation, a statistical equation for the kinetics of gas molecules, instead of solving directly the Navier-Stokes equations. As detailed in Refs.[17,18], the governing equations consider the probability $f_i(x, t)$ to have a set of particles at location x and time t, with a velocity c_i:

$$f_i(x + c_i\delta t, t + \delta t) = f_i(x, t) + \Omega_{ij}(x, t) \tag{5}$$

for $[0 < i, j < N]$, where c_i is a discrete velocity of a set of N velocities and Ω_{ij} is an operator representing the internal collisions of pairs of particles. In this work, the kinetic scheme is based on a D3Q27 formulation, that ensures the conservation of mass and momentum. The collision operator is represented by a single relaxation time model and a regularisation technique is applied to increase the stability and accuracy of the method[19,20]. The regularization step ensures a LES formulation without subgrid scale model[21].

Previous works[22] have shown that the convergence of thrust and torque requires to achieve a grid resolution corresponding to $\Delta x/C = 0.01 - 0.015$. The dimension of the first cell in the direction normal to the wall is thus set to $\Delta x/C = 0.015$, corresponding to $\overline{y^+} \approx 50$. Far from the wall the cell size is increased, by means of a hierarchical grid refinement approach with 5 grid levels (from one grid to the next grid, both the time step and the spatial step is increased by a factor 2). The total number of grid points for the full mesh is 143.5×10^6 (with 50% of the points located in the vicinity of the rotor disk in the first grid level). A full rotation of the rotor is discretized with 20,100 time steps. The typical computational time needed to achieve one rotation of the rotor is 1500hCPU (with 120 cores of a classical supercomputer). About 10 rotations are simulated to achieve a stabilised operating point.

3. MODELLING OF FLUID-STRUCTURE INTERACTIONS (FSI)

3.1. Development of FSI capabilities

A monolithic aero-elastic flow solver is developed, to maintain the computational performance of the LBM code. The approach relies on the use of generalised coordinates to represent each blade of the rotor as a flexible beam. As a first step a simple dynamical model is considered, based on a classical second order dynamic model for the structure deformation, as:

$$I_q \frac{\mathrm{d}^2 q(t)}{\mathrm{d}t^2} + D_q \frac{\mathrm{d}q(t)}{\mathrm{d}t} + K_q q(t) = M_q(t) \tag{6}$$

with q a generalised coordinate of the system, I_q the moment of inertia with respect to the axis of rotation of the coordinate q, D_q a damping factor, K_q the stiffness of the structure and M_q the sum of external moments applied to the system with respect to the axis of rotation of coordinate q. Three generalised coordinates are used to represent the displacement of the blade:

1. Pitching angle α around the spanwise axis located a quarter chord away from the leading edge (corresponding to the aerodynamic center). The corresponding angular velocity is noted $\dot{\alpha}$ in Fig. 3(a),
2. Flapping angle β around the blade hinge, horizontal, perpendicular to the spanwise axis and with its origin at the rotor hub. Flapping angular velocity is noted $\dot{\beta}$ in Fig. 3(b),
3. Surging angle ω around the main rotor axis. The angular velocity is noted $\dot{\omega}$ in Fig. 3(c) (this movement corresponds to a variation of the rotation speed Ω).

The integration of Eq. 6 recovers the previous quantities, which combined with the main rotational velocity Ω, returns the absolute angular velocity of each discrete surface point.

3.2. Numerical implementation

To impose the unsteady displacement of the blade, the following algorithm is implemented in the flow solver:

1. after the calculation of equilibrium distributions and before the collide and stream steps, every Lagrangian surface particle is assigned with a velocity function and all forces on the particles are reset to zero,

2. particles are advanced everywhere to their new position and
3. the immersed boundary algorithm is applied until the compatibility criterion is met (following an iterative process that requires typically 4 to 6 iterations).

3.3. Determination of the velocity functions

Typically, two types of velocity function can be imposed: (a) a forced motion (the kinematic of the blade is know *a priori* so it is not necessary to solve Eq. 6) and (b) dynamic response which requires to solve Eq. 6 to know the new displacement velocity of the blade.

3.3.1. Forced motion

The forced motion model imposes a periodic motion around a secondary axis (e.g. hinge, spanwise axis or in the case of surging, the same rotor axis) that is superimposed to the main rotation of the blade. This approach is similar to the one presented in Ref.[23]. A sinusoidal angular velocity $\dot{q}$ is chosen for the corresponding generalized coordinate:

$$\dot{q} = -\omega_m q_{max} cos(\omega_m t) \quad (7)$$

where ω_m is the motion frequency and q_{max} the amplitude of the motion. The velocity function given to Lagragian points corresponds to the sum of the velocities due to the two successive rotations, with angular velocities Ω and $\dot{q}$ in a single time step.

3.3.2. Dynamic response

The model solving the dynamic interaction between the fluid and the structure requires to integrate Eq. 6, which is done using a fourth-step Runge-Kutta scheme. This integration is performed at the coarsest level of the numerical simulation whereas the immersed boundary algorithm is updated at the finest level. This results in a constant angular acceleration at the chosen generalized coordinate during the whole "coarse" time step duration and the angular velocity of the chosen generalized coordinate evolves linearly. Introducing the state variable $\boldsymbol{Q} = [q\dot{q}]$ and rearranging Eq. 6, a system of first order is retrieved:

$$\frac{\mathrm{d}}{\mathrm{d}t}\boldsymbol{Q} = \begin{bmatrix} \dot{q} \\ \frac{M}{I} - \frac{K}{I}q - \frac{D}{I}\dot{q} \end{bmatrix} \quad (8)$$

The inertia, damping, stiffness and force terms are respectively (in the case of rotation): mass moment of inertia, rotational damping, rotational stiffness and torque around the axis of rotation.

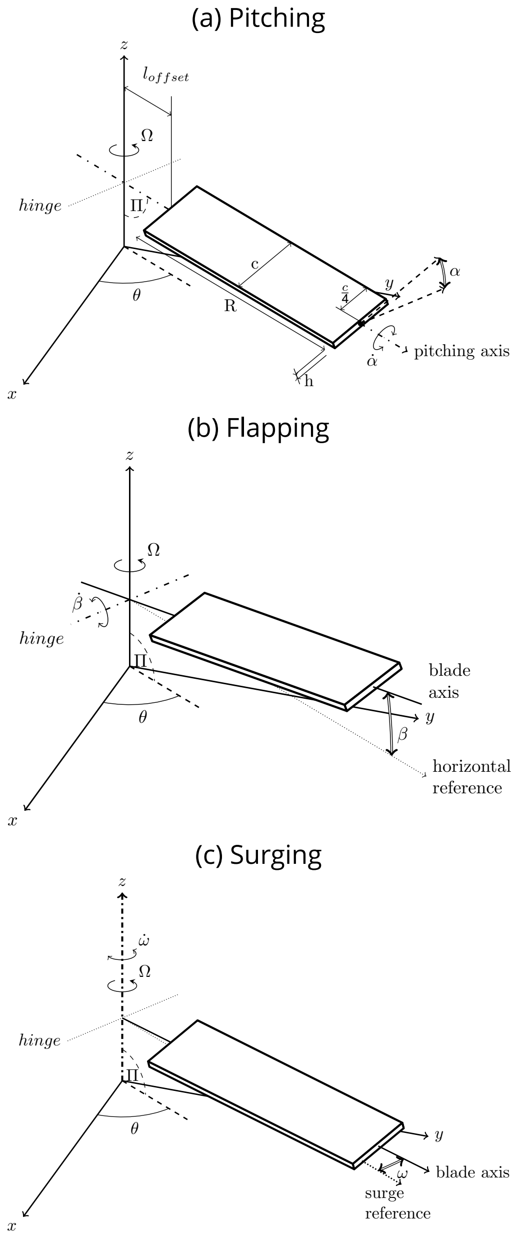

Figure 3: View of the generalized coordinate system used to describe the blade movement: (a) pitching model with offset l_{offset} with respect to the main rotation axis, (b) flapping model (the blade rotates around the hinge) and (c) surging model (the blade rotates with a non-constant rotational speed).

4. VERIFICATION AND VALIDATION

A first step is to validate the capability of the LES-LBM approach to estimate: 1) the global performance of the rotor compared to experimental data and 2) the main effect of forced motion compared to URANS predictions. The torque and thrust coefficients, C_Q and C_T, are defined as

$$C_T = \frac{\overline{T}}{\frac{1}{2\times16}\rho(\Omega.D)^2\pi D^2}, \quad (9)$$

and

$$C_Q = \frac{\overline{Q.\Omega} + \overline{Q_i.\dot{\omega}_i}}{\frac{1}{2\times32}\rho\Omega^3\pi D^5}. \quad (10)$$

To allow a fair comparison between all the configurations in the case of forced motion, the torque coefficient takes into account for two contributions: a) the power needed to impose the rotation, $P_\Omega = \overline{Q.\Omega}$ and b) the power to impose the secondary motion $P_{\dot{\omega}} = \overline{Q_i.\dot{\omega}_i}$ (with Q_i and $\dot{\omega}_i$ the instantaneous torque and displacement velocity related to the forced motion).

The evolution of C_Q with respect to C_T is shown in Fig. 4 for two configurations: a) the reference configuration (constant rotation speed) and b) a case where a forced motion of pitching is superimposed to the rotational speed ($\omega_m = 3\Omega$, $q_m = 0.1724$, corresponding to a variation of $\pm 9.9^o$ around the average pitch angle). For the reference configuration, the discrepancy on thrust between URANS, LES-LBM and measurements is 7% and 14% respectively. However, both URANS and LES-LBM correctly estimate the C_Q/C_T ratio. The figure of merits are 0.611 (measurements), 0.647 (URANS) and 0.616 (LES-LBM). Despite the differences with measurements on the thrust coefficient, this comparison validate the capability of LES-LBM to predict the rotor performance.

For the case with a forced pitching motion, URANS predicts an increase of the thrust and torque by 1% and 24%, respectively. For the same configuration, LES-LBM predicts an increase of the thrust and torque by 4% and 21%, respectively, which is in good agreement with the URANS results. This comparison is satisfying, since the flow is affected with alternative separation and reattachment phases, which are known to be challenging to predict for numerical simulations.

The conclusion of this section is that LES-LBM is able to predict the effect of complex motion, like pitching, on the rotor performance (at least qualitatively). The comparison with measurements in terms of figure of merit is also satisfying with less than 1% of error.

(a) Reference

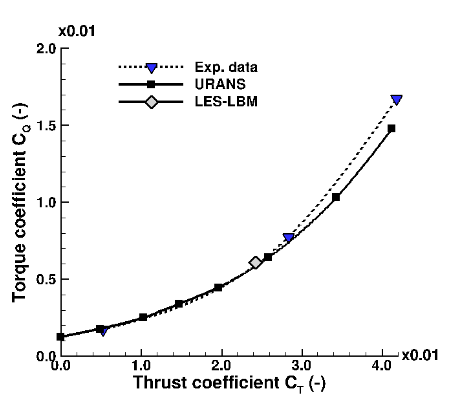

(b) Pitching motion

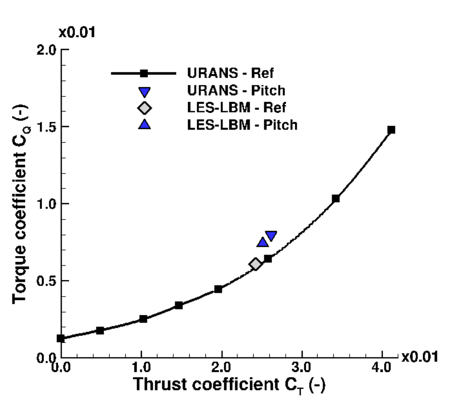

Figure 4: Prediction of the torque coefficient C_Q with respect to the thrust coefficient C_T: (a) comparison with measurements, (b) comparison of the pitching motion influence with URANS predictions.

5. FORCED MOTION

5.1. Influence on the rotor performance

The three kind of solid rotations (pitching, flapping and surging) have very different effects on the flow that is seen by the blade. A scheme is shown in Fig. 5 to explain how each forced motion will modify the flow condition seen by the blade. As indicated by Eq. 7, if only harmonic motions are considered, each elementary motion depends on only two parameters: the amplitude q_{max} and the frequency ω_m. The forced motion frequency can then be compared to a characteristic frequency of the flow (e.g. based on the time needed to travel from the leading edge to the trailing edge of the blade) to define a reduced velocity U^* as:

$$U^* = \frac{\Omega . r_{mid}}{\omega_m C}, \tag{11}$$

with r_{mid} the radius at midspan. To ensure interactions between the forced motion and the flow, the value of U^* should be of the magnitude order of 1: for $U^* \ll 1$ the flow does not have the time to adapt (the forced motion effects will be filtered by the flow), while for $U^* \gg 1$, the flow will adapt very rapidly compared to the forced motion velocity, corresponding to a succession of quasi-steady states.

The simplest forced motion is the pitching motion, Fig. 5(a): the blade rotate around its center located at quarter-chord, so the flow conditions at the inlet alternatively vary between $(\alpha_0 - \Delta\alpha)$ and $(\alpha_0 + \Delta\alpha)$. The effect of the parameter q_{max} is to directly set the minimum and maximum angles that will be seen by the blade. The influence of the frequency ω_m is more subtile: by inducing an angular speed at the leading edge, it modifies the effective angle of attack seen by the profile. This effect is added to the geometric blade angle.

The flapping is a complex motion composed of two parts, Fig. 5(b): first a downstroke movement, where the blade moves in the same direction than the induced velocity, then an upstroke movement, where the blade moves in the direction opposite to the induced velocity. Since the flapping motion corresponds to a rotation around the hinge, a part of the flapping velocity component is added (downstroke) or deducted (upstroke) from the main rotational speed. The result is that, as for the pitching case, this movement is not exactly symmetric regarding the variation of the angle of attack. If the velocity of the blade displacement is higher than the induced velocity, this would result in an inversion of the suction and pressure sides.

The surging motion corresponds to a variation of the rotational speed, Fig. 5(c). Alternatively the

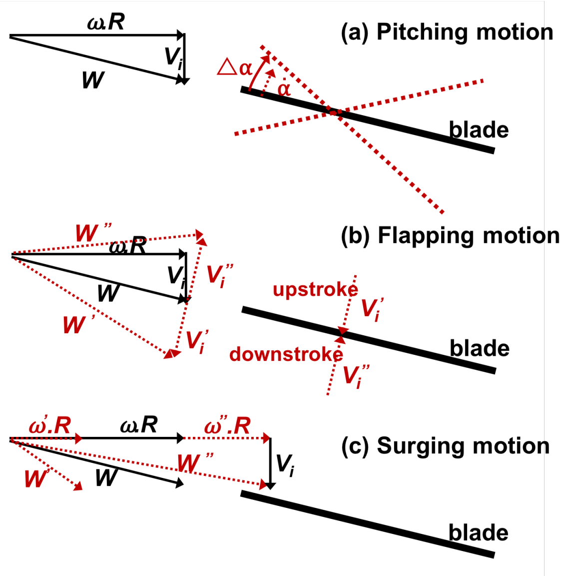

Figure 5: Explanation of the influence of the three different forced motion on the flow conditions seen by the blade: (a) pitching, (b) flapping and (c) surging. The induced velocity is noted V_i.

blade decelerates, then accelerates. As shown on the scheme, assuming a constant induced velocity that is lower than the rotational speed, the effect of the deceleration on the angle of attack is more important than the effect of the acceleration. During the deceleration and acceleration phases, the angle of attack is decreased and increased, respectively.

An efficient comparison of the three motions is not straightforward, since it requires to know *a priori* the value of the induced velocity (that depends on the global performance of the rotor). Assuming that one of the most important parameter is the variation of the angle of attack, an effort has been done to ensure that this parameter remains of the same magnitude order when comparing all three motions.

The parameters used for each of the three forced motions are indicated in Table 3. A frequency corresponding to a reduced velocity of 1.0 has been chosen for all forced motions to ensure a contribution of unsteady flows to the rotor performance.

Table 3: Parameters of the forced motions.

	Pitch	Flap	Surge
Amplitude q_{max}, rad	0.1724	0.0912	0.2314
Frequency ω_m, rad/s	3Ω	3Ω	3Ω
Reduced velocity U^*	1.0	1.0	1.0

The effect on the torque and thrust coefficients

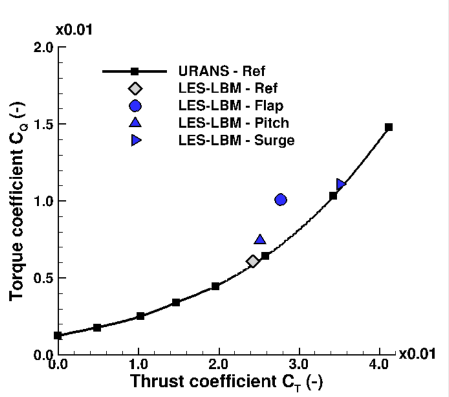

Figure 6: Comparison of the torque coefficient C_Q with respect to the thrust coefficient C_T obtained by imposing different forced motions (the reference case corresponds to a pure steady rotation case).

is shown in Fig. 6. The three different motions lead to an increase of the thrust for the same rotation speed Ω, by +4%, +14% and +45% for the pitching, flapping and surging motion, respectively. However, a penalty on the torque is observed for all three motions, compared to the pure rotation case. The data reported in Table 4 show that except in the case of pitching, the power needed to actuate the blade and impose the forced motion is found to be significant (around 40% in the case of flapping and surging). This means that some improvements could be done to optimise the kinematics of the blade and reduce this penalty. In the case of surging, the penalty is moderate compared to the increase in thrust (the new operating point is close to an operating point corresponding to $\alpha = 20^o$).

Table 4: Contributions to the torque coefficient.

	Pitch	Flap	Surge
Total torque coefficient	0.0074	0.0101	0.0111
due to rotation	99%	61%	55%
due to the forced motion	1%	39%	45%

The increase of thrust is correlated to the periodic variation of the angle of attack as shown in Fig. 7. For the reference case, the thrust coefficient variation is around 0.001. In the case of forced motion, the thrust coefficient varies by ± 0.034, ± 0.021 and ± 0.038 in the case of pitching, flapping and surging, respectively. In the case of pitching, the time lag between the variation of the angle of attack and the variation of the thrust is about 0.1T, with T the period of revolution of the rotor, which is similar to the time that a particle needs to travel from the leading edge to the trailing edge. The same time lag (0.1T) is observed in the case of flapping, which corroborates the use of $\Omega.r/C$ as the characteristic frequency of the flow to compare with the frequency of the forced motion. In the case of surging, the thrust varies fully in phase with the rotation speed.

Instantaneous flow fields related to the reference case are shown in Fig. 8. An intense leading edge vortex develops along the blade span, leading to a massive separation close to the blade tip. Such flow phenomenon has already been reported in the literature for similar low Reynolds number rotors[15,24,25]. The picture shown in Fig. 8(b) confirms that the flow is fully separated at $r/R = 0.8$, generating intense vortices behind the trailing edge. These vortices actually generate a high level of turbulent activity that impacts the leading edge of the following blade.

5.1. Pitching motion

Instantaneous flow fields for the pitching case are plotted in Fig. 9 at four different instants, describing a period of time associated to the pitching motion (corresponding to a third of the rotor revolution). The flow in Fig. 9(a) corresponds to the highest value of angle of attack ($\alpha = \alpha_0 + \Delta\alpha \approx 25^o$). As expected, the boundary layer on the suction side is fully separated. When the incidence is progressively reduced, the flow reattaches completely. However, the influence of the leading edge vortex is still visible, even at the lowest incidence. When the blade returns to its original position $\alpha = \alpha_0$, Fig. 9(d), the intensity of the leading edge vortex re-increases. This vortex is then ejected towards the trailing edge when the incidence is further increased. The behaviour of this leading edge vortex is responsible for the moderate increase of the thrust coefficient, compared to the reference case.

5.2. Flapping motion

Instantaneous flow fields for the flapping case are plotted in Fig. 10 at four different instants, describing a period of time associated to the flapping motion. The flow in Fig. 10(a) corresponds to the beginning of the downstroke step of the motion. At this position, the intensity of the leading edge vortex is reduced compared to the reference case. During the downstroke step, Fig. 10(b), the blade experiences large angle of attacks ($\alpha = \alpha_0 + \Delta\alpha \approx 30^o$), which results in a large separation in the vicinity of the blade tip as well as the periodic emission of coherent flow patterns at the trailing edge. The separation is amplified at the beginning of the upstroke motion, Fig. 10(c), where the boundary layer on the suction side is separated on the full blade span.

(a) Pitching

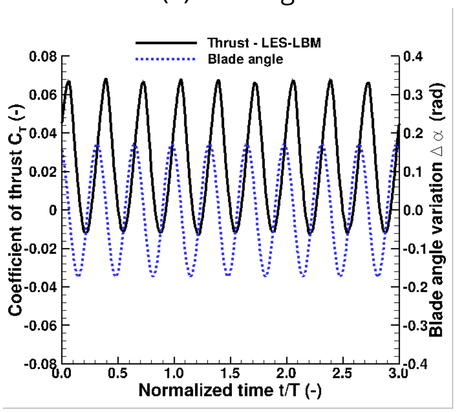

(b) Flapping

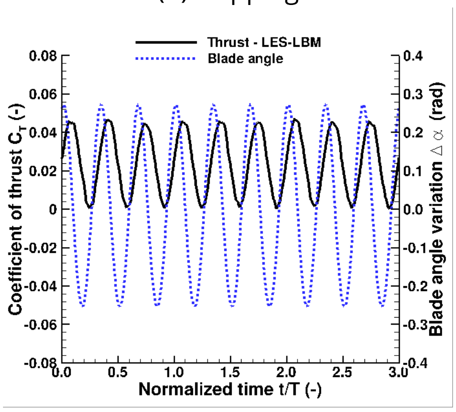

(c) Surging

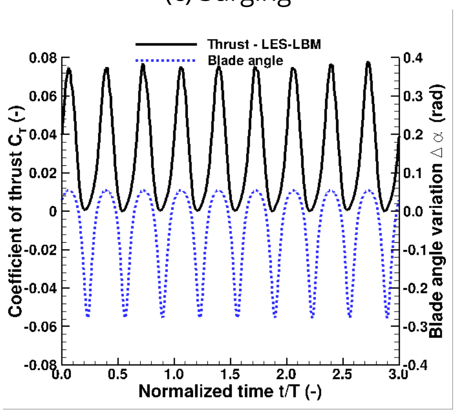

Figure 7: Correlation between the thrust coefficient C_T and the variation of the angle of attack seen by the blade (at r/R=0.8): (a) pitching, (b) flapping and (c) surging.

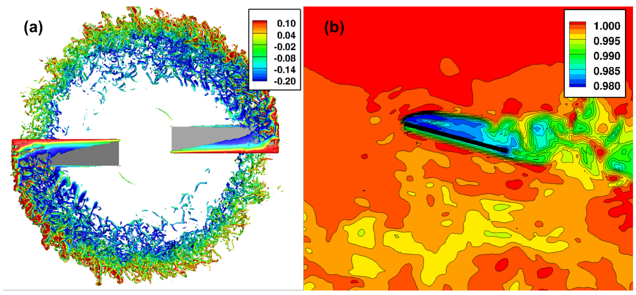

Figure 8: Instantaneous flow fields for the reference case: (a) iso-surface of Q-criterion coloured with the normalised streamwise velocity $V_z/(\Omega.R)$ and (b) slice at $r/R = 0.8$ coloured with the total pressure.

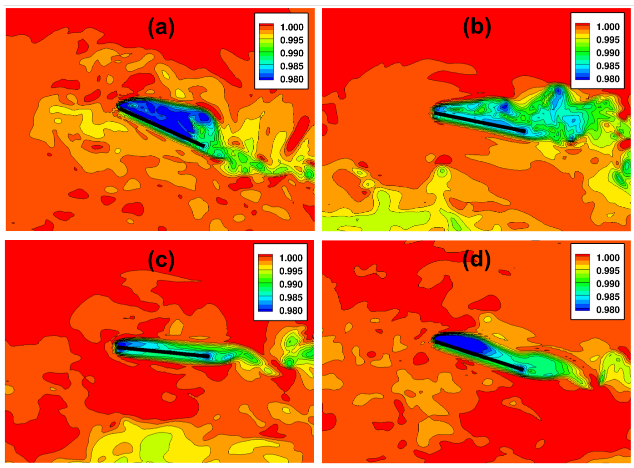

Figure 9: Instantaneous flow fields at four different instants, for the pitching case: slice at $r/R = 0.8$ coloured with the total pressure.

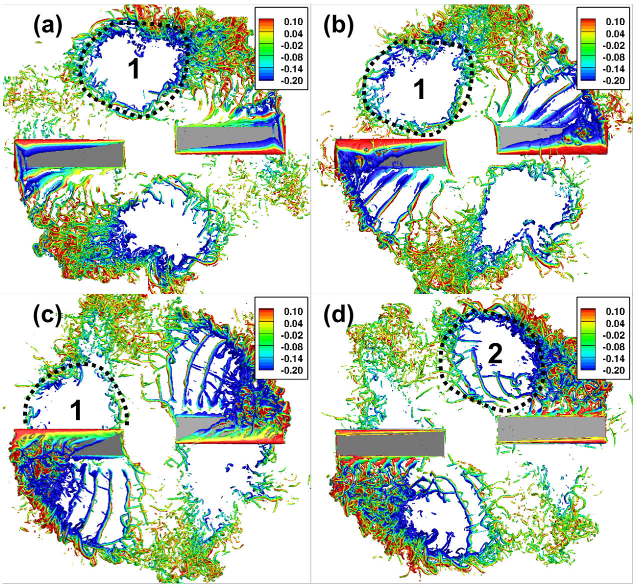

Figure 10: Instantaneous flow fields at four different instants, for the flapping case: iso-surface of Q-criterion coloured with the normalised streamwise velocity $V_z/(\Omega.R)$. The zones noted 1 and 2 correspond to the typical patterns generated by the blades at the beginning of the upstroke step.

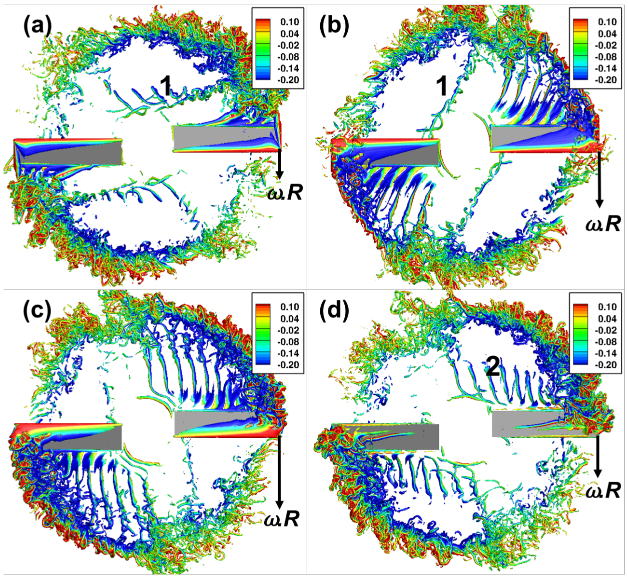

Figure 11: Instantaneous flow fields at four different instants, for the surging case: iso-surface of Q-criterion coloured with the normalised streamwise velocity $V_z/(\Omega.R)$. The velocity vectors close to the blade tip are added to the figure to identify the corresponding step of the superimposed motion.

During the upstroke step, the typical movement of the blade creates some regions in the flow, noted 1 and 2 in Fig. 10, where there is no turbulent activity. These particular flow patterns are then convected with the flow and are still observable after half a rotation of the rotor.

5.3. Surging motion

Instantaneous flow fields for the surging case are plotted in Fig. 11 at four different instants, describing a period of time associated to the surging motion. The flow in Fig. 11(a) corresponds to the lowest rotational speed. At this position, the intensity of the leading edge vortex is reduced compared to the reference case and no separation is observed close to the rotor tip. During the acceleration step, Fig. 11(b), the blade experiences a moderate increase of the angle of attack ($\alpha = \alpha_0 + \Delta\alpha \approx 18^o$), which results in an increase of the intensity of the leading edge vortex, and the beginning of a separation process at the tip. When the blade achieves its maximum rotation speed ($\Omega + q_{max}.3\Omega \approx 1.69\Omega$), the separation is amplified at the rotor tip, Fig. 11(c), and the activity of the leading edge vortex starts to decrease. During the last instant, Fig. 11(d), when the rotor speed is returned close to its nominal speed Ω, the leading edge vortex is ejected towards the trailing edge. This phenomenon is due to the inertie of the flow that is rotating at a higher speed than the rotor, so the leading edge vortex, previously attached to the blade, is blown by the flow. This process is shown in Fig. 11 by following the zone noted 1 (then 2 at the beginning of a new cycle). Together with the periodic increase of the rotational speed, this process is responsible for the increase of the thrust coefficient.

To separate the effect related to the increase of the rotational speed (steady effect) from the unsteady flow effect, it is possible to estimate what the thrust evolution in time should be in the case of a quasi steady approach. Knowing the thrust coefficient for the reference velocity Ω, the quasi steady thrust coefficient is estimated as

$$C_T(t) = \overline{C_T} \times \frac{(\Omega + q_{max}.\dot{\omega}cos(\dot{\omega}t))^2}{(\Omega)^2} \tag{12}$$

with $\dot{\omega} = 3\Omega$. Based on this approximation, the quasi-steady thrust is compared with the thrust observed during the surging simulation in Fig. 12. The difference between both curves corresponds to an estimate of the unsteady flow effects. This comparison shows that most of the increase in thrust during surging is related to a quasi-steady effect. Unsteady flow effects are however responsible for an additional increase of the thrust when the rotor achieved its maximum rotational speed.

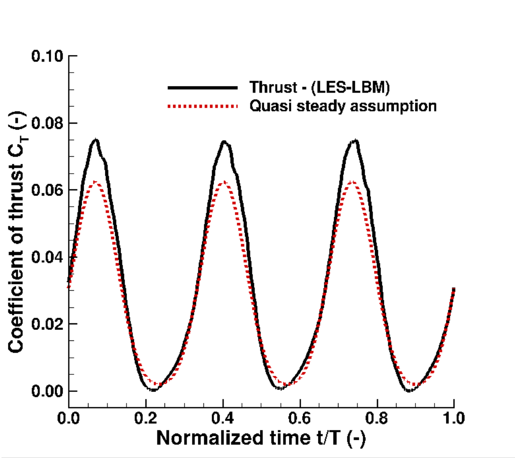

Figure 12: Comparison of the observed thrust coefficient C_T in the case of surging with an estimation based on a quasi-steady assumption.

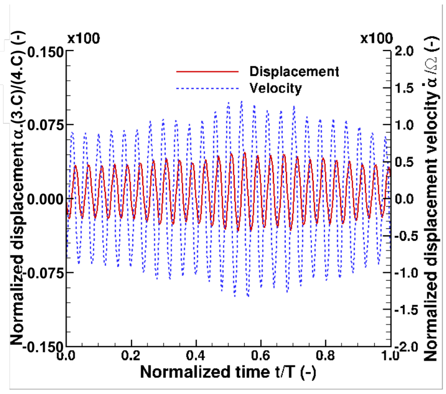

Figure 13: Normalised displacement and normalised velocity of displacement registered at the blade trailing edge, during the coupled resolution of the flow with the dynamic pitching mode.

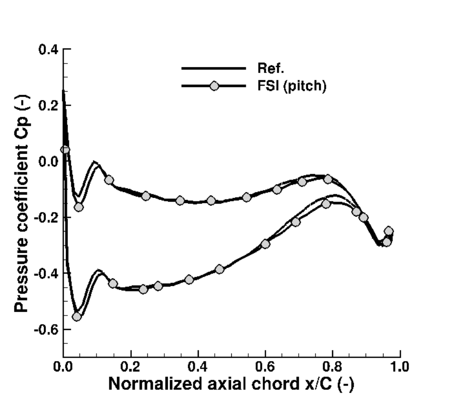

Figure 14: Time averaged pressure coefficient at 80% of the rotor span, $r/R = 0.80$, showing the influence of FSI on the pressure profiles.

6. DYNAMIC RESPONSE MOTION

The last section of this paper is dedicated to the resolution of the flow coupled with the dynamic response of the blades. The relation in Eq. 6) is solved for each blade, so each blade is independent from the other and free to react to the aerodynamic forces. The values reported in Table 2 are used to investigate two cases: pure dynamic pitching and pure dynamic flapping.

6.1. Coupling with pitching

The coupled resolution is activated only after one full revolution of the rotor, in order to avoid the large oscillations of the force that are associated with the first part of the transient regime. The normalised displacement and the normalised velocity displacement are plotted for the last rotation of the simulation, Fig. 13. Two conclusions are drawn: first, the blade oscillations are periodic in time, with a frequency close to the resonance frequency of the blade, defined as

$$f_{\alpha,\beta} = \frac{1}{2\pi}\sqrt{\frac{K_{\alpha,\beta}}{I_{\alpha,\beta}}}. \tag{13}$$

Then, after the transient regime, the oscillations are nor damped or amplified. A residual oscillation, corresponding to less than 0.02 degrees of angle of attack, remains associated to the blade. When considering the natural frequency of the blade ω_α, the value of the reduced velocity U^*(see Eq. 11) is found to be 1.33. This means that a coupling between the flow and the blade is possible since their respective behaviours are related to the same range of frequency. An effect of less than 0.5% on the thrust and torque coefficients is observed.

The pressure coefficient defined as $C_p = 2(p - p_0)/(\rho.(\Omega.D/2)^2)$, is plotted in Fig. 14 at $r/R = 0.80$. As expected, the main effect is observed close to the trailing edge. On the rear part of the profil (x/C=0.8), a small decrease of the flow deflection is pointed out, which is responsible for the small variation of the torque and thrust coefficients.

6.2. Coupling with flapping

The simulation is now run in a coupled fashion considering the flapping mode. The normalised displacement and the normalised velocity displacement are plotted in Fig. 15. Contrary to the pitching case, that shows a periodic undamped signal, the flapping motion is rapidly damped in less than half a rotation. Very small oscillations are still ob-

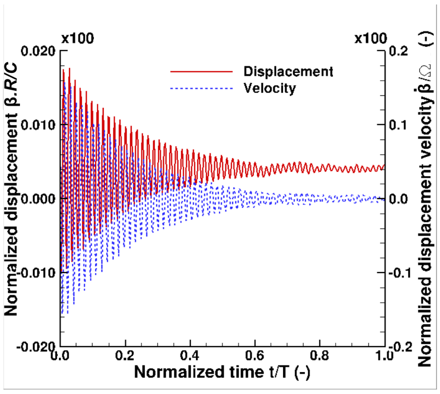

Figure 15: Normalised displacement and normalised velocity displacement registered during the coupled resolution of the flow with the dynamic flapping mode.

served after many rotations, but they have no effect on the rotor performance. A new equilibrium position is found, very close to the uncoupled case, corresponding to an unsignificant deflexion of 0.003% of the chord in the opposite direction compared to the induced flow. When considering the natural frequency of the blade ω_β, the value of the reduced velocity U^*(see Eq. 11) is found to be 0.46, which is significantly lower than 1. This explains the limited interaction between the dynamic flapping and the flow.

7. CONCLUSION

Fluid-Structure Interactions capabilities have been implemented in a LBM code, based on the use of an immersed boundary approach. The flow solver is coupled in a monolithic way with the dynamic equation, considering a simple beam approximation for the blades. These new capabilities can also be used to impose a new kinematics based on pitching, flapping or surging, that is superimposed to the rotation of the blades. Regarding FSI, the dynamic pitching has more influence than the dynamic flapping. This is mainly due to the natural frequency associated with pitching that is closed to the typical frequency encountered in the flow. However, in both cases, the influence of vibrations is very small (flapping has no influence on the rotor performance, while pitching reduces the thrust by less than 1%).

The different forced motions imposed to the rotation show much significant influence on the rotor performance. Pitching, flapping and surging lead to an increase of the thrust coefficient, at the price of a penalty on the torque that completely balance the advantage on the thrust. Among these forced motions, surging and flapping are promising candidates. A margin of improvement can still be expected to reduce the overcost on the torque (about 40% of the power is required to power the flapping or surging motion).

Perspectives to this work incluse the study of more complex motions, considering a combination of many angular velocities. Regarding FSI, future works will focus on more flexible blades (higher aspect ratio or lower stiffness).

ACKNOWLEDGEMENTS

Numerical simulations have been performed thanks to the computing center of the Federal University of Toulouse (under projects CALMIP p1425 and p17014) and resources provided by GENCI (project A0042A07178). These supports are greatly acknowledged. Special thanks to Jonas Latt, from the University of Geneva and FlowKit, for their support on Palabos. The authors also thank the development team of Antares (http://cerfacs.fr/antares) at CERFACS, for providing the software used for post-processing.

REFERENCES

[1] T. Theodorsen. General theory of aerodynamic instability and the mechanism of flutter. Technical Report NACA-TR-496, NACA, 1935.

[2] J. M. Greenberg. Airfoil in sinusoidal motion in pulsating stream. Technical Report NACA TN 1329, NACA, 1947.

[3] T. van Holten. A single rotor without reaction torque : a violation of newton's laws or feasible? In *28th European Rotorcraft Forum*, 2002.

[4] B. Fitchett and I. Chopra. A biologically inspired flapping rotor for micro air vehicles. In *AHS international specialists' meeting on unmanned rotorcraft*, pages 23–25, 2007.

[5] S. Guo, D. Li, and J. Wu. Theoretical and experimental study of a piezoelectric flapping wing rotor for micro aerial vehicle. *Aerospace science and technology*, 23:429–438, 2012.

[6] J. Wu, D. Wang, and Y. Zhang. Aerodynamic analysis of a flapping rotary wing at a low reynolds number. *AIAA J.*, 53:2951–2966, 2015.

[7] J. Wu, C. Zhou, and Y. Zhang. Aerodynamic power efficiency comparison of various micro-air-vehicle layouts in hovering flight. *AIAA J.*, 55(4):1265–1278, 2017.

[8] H. Li, S. Guo, Y. L. Zhang, C. Zhou, and J. H. Wu. Unsteady aerodynamic and optimal kinematic analysis of a micro flapping wing rotor. *Aerospace science and technology*, 63:167–178, 2017.

[9] S. Guo, H. Li, C. Zhou, Y. L. Zhang, Y. He, and J. H. Wu. Analysis and experiment of a bio-inspired flyable micro flapping wing rotor. *Aerospace science and technology*, 79:506–517, 2018.

[10] L. Chen, J. Wu, C. Zhou, S. J. Hsu, and B. Cheng. Unsteady aerodynamics of a pitching-flapping-perturbed revolving wing at low reynolds number. *Physics of Fluids*, 30(5):051903, 2018.

[11] D. Wang, J. Wu, and Y. Zhang. Effects of geometric parameters on flapping rotary wings at low reynolds numbers. *AIAA J.*, 56(4):1372–1387, 2018.

[12] J. Wu, L. Chen, C. Zhou, S. J. Hsu, and B. Cheng. Aerodynamics of a flapping-perturbed revolving wing. *AIAA J.*, 2018.

[13] T. Jardin, N. Doue, S. Prothin, and J. M. Moschetta. Numerical analysis of pitching-rotor aerodynamics. *J. of Fluids and Structures*, 62:172–186, 2016.

[14] A. R. Abdulghany. Generalization of parallel axis theorem for rotational inertia. *American Journal of Physics*, 85(791), 2017.

[15] N. Gourdain, D. Singh, T. Jardin, and S. Prothin. Analysis of the turbulent wake generated by a micro-air vehicle hovering near the ground with a Lattice Boltzmann Method. *J. American Helicopter Society*, 64(2):1–15, 2017.

[16] T. Inamuro. Lattice boltzmann methods for moving boundary. *Fluid Dyn. Res.*, 44(2):024001, 2012.

[17] P. Lallemand and L. S. Luo. Theory of the lattice Boltzmann method: dispersion, dissipation, isotropy, Galilean invariance, and stability. *Phys. Rev. E.*, 61(6):6546–6562, 2000.

[18] D. D'Humieres, I. Ginzburg, M. Krafczy, P. Lallemand, and L. S. Luo. Multiple relaxation time lattice Boltzmann models in three-dimensions. *Phil. Trans. R. Soc. A*, 360(1792):437–451, 2002.

[19] J. Latt and B. Chopard. Lattice Boltzmann method with regularized non-equilibrium distribution functions. *Math. Comp. Sim.*, 72:165–168, 2006.

[20] O. Malaspinas, B. Chopard, and J. Latt. General regularized boundary condition for multi-speed lattice boltzmann models. *J. Computer and Fluids*, 49:29–35, 2011.

[21] P. Sagaut. Toward advanced subgrid models for lattice Boltzmann based large-eddy simulation: theoretical formulations. *Computers and mathematics with applications*, 59(7):2194–2199, 2010.

[22] N. Gourdain, T. Jardin, R. Serre, S. Prothin, and J.-M. Moschetta. Application of a lattice boltzmann method to some challenges related to micro-air vehicles. *International J. of Micro Air Vehicles*, to be published.

[23] D. J. Van Gerwen and T. Van Holten. A new apporach to forced flapping for the ornicopter. In *26th International Congress of the Aeronautical Sciences (ICAS)*, 2008.

[24] C. J. Wojcik and J. H. J. Buchholz. Parameter variation and the leading-edge vortex of a rotating flat plate. *AIAA J.*, 52(2):348–357, 2014.

[25] D. J. Garmann and M. R. Visbal. Dynamics of revolving wings for various aspect ratios. *J. of Fluids Mechanics*, 748(3):932–956, 2014.